A Novel One-Step Hydrothermal Preparation of Ru/$Sn_xTi_{1-x}O_2$ Diesel Oxidation Catalysts and its Low-Temperature Performance

Li Fan, Qi Sun, Wei Zheng, Qinyuan Tang, Ting Zhang and Mengkui Tian[*]

Abstract

The rutile $Sn_xTi_{1-x}O_2$ (x = 0, 0.33, 0.5, 0.67, 1) solid solution was synthesized by a one-step hydrothermal method, in which tetrabutyl titanate and Tin (IV) chloride pentahydrate were used as raw materials. A series of Ru/$Sn_xTi_{1-x}O_2$ were then prepared by the impregnation process in $RuCl_3$ to investigate the performance and stability of CO and C_3H_8 oxidation. These catalysts were characterized through XRD, N_2 adsorption-desorption, FT-IR, TEM, XPS, H_2-TPR, and O_2-TPD techniques. The effect of Sn/Ti molar ratio and hydrothermal condition on the low-temperature catalytic oxidized performance and stability of Ru/$Sn_xTi_{1-x}O_2$ were investigated. The results indicated that Ru/$Sn_{0.67}Ti_{0.33}O_2$ catalyst showed an excellent activity and stability at low temperatures. The CO conversion reached 50% at 180 °C and 90% at 240 °C. Besides, the C_3H_8 conversion reached 50% at 320 °C, the complete conversion of C_3H_8 realized at 500 °C, and no deactivation occurs after 12 h of catalytic reaction. The excellent low-temperature activity and stability of the Ru/$Sn_{0.67}Ti_{0.33}O_2$ were attributed to the following factors. Firstly, XRD results showed that Sn^{4+} was successfully introduced into the lattice of TiO_2 to replace Ti^{4+} forming a homogeneous solid solution (containing $-Sn^{4+}-O-Ti^{4+}-$ species), which was consistent with TEM and N_2 adsorption-desorption results. The introduction of Sn could suppress the growth of anatase crystal and promote the formation of rutile phase, and this phase transition was helpful to improve the low-temperature activity of the catalysts. Secondly, TEM images showed that ultrafine Ru nanoparticles (~ 5 nm) were dispersed on $Sn_{0.67}Ti_{0.33}O_2$ support, suggesting that the formation of $Sn_xTi_{1-x}O_2$ solid solution was beneficial to the dispersion of Ru particles.

Keywords: Solid solution, Rutile, One-step hydrothermal method, Low-temperature activity, Stability

Background

Diesel engines are widely applied in the field of transportation, mining, and engineering machinery due to these advantages of low fuel consumption, high thermal efficiency, and good stability [1]. However, carbon monoxide (CO), unburned hydrocarbons (HCs), various oxides of nitrogen (NO_x), and the particulate matter (PM) in diesel vehicle exhaust have caused a serious threat to ecological environment and human health [2, 3]. Furthermore, stringent

environmental laws and regulations have driven recent advances in diesel emission control technologies. An integrated exhaust after-treatment system consisting of diesel oxidation catalyst (DOC), selective catalytic reduction (SCR), and catalyzed diesel particulate filter (DPF) has been widely used to purify diesel exhausts. The functions of the DOC in the after-treatment system are converting CO, HCs, and NO into CO_2, H_2O, and NO_2, the NO_2 being used as raw material for subsequent de-NO_x reaction to promote SCR reaction. In addition, it could also oxidize the soluble organic fraction (SOF) to decrease PM emissions. HCs excessive emission will be caused owing to the

* Correspondence: tianmk78@126.com
School of Chemistry and Chemical Engineering, Guizhou University, Guiyang 550025, China

incomplete combustion of HCs during the cold start of diesel vehicles. Therefore, the catalysts need to ignite rapidly at low temperatures [4]. Presently, noble metal catalysts (such as Pt, Pd, and Rh) supported on carbon materials or oxides (such as TiO_2, Al_2O_3, CeO_2, and ZrO_2) are commercialized diesel oxidation catalysts with good performance for CO, NO, and HCs catalytic oxidation. However, there are drawbacks to commercialized catalysts, such as poor thermal stability, strong self-inhibition by CO, and high cost [5].

Ru and RuO_x catalysts are widely applied in oxidizing CO [6], methane [7], and chlorobenzene [8]. Importantly, Ru catalysts have excellent low-temperature activity and poison resistance [8–11]. But Ru and RuO_x are easily sintered, resulting in active sites' exposure decreases [12]. Therefore, Ru catalysts should be supported on a carrier to prevent their sintering and improve catalytic activity.

TiO_2 has been widely used to purify diesel exhausts. RuO_x and rutile phase TiO_2 have a similar lattice constant, and the rutile TiO_2 in Ru/TiO_2 catalysts plays an important role in stabilizing RuO_x particles during calcination process in comparison with anatase-supported RuO_x catalysts. Therefore, RuO_x can be highly dispersed on the surface of TiO_2. Furthermore, there is a synergistic effect between RuO_x and TiO_2, which is beneficial to improve the redox ability of Ru/TiO_2 [13–18]. In order to further improve the thermal stability, dispersion of active components, and transformation of anatase to rutile phase, many studies have introduced Sn^{4+} into TiO_2 to form $Sn_xTi_{1-x}O_2$ solid solution. Huang et al. [16] found that the introduction of Sn^{4+} into TiO_2 lattice could improve the stability of the $CuO/Ti_xSn_{1-x}O_2$ catalysts and dispersion of CuO. Bai et al .[17] indicated Sn^{4+} significantly improved the thermal stability of TiO_2. Mehraz et al. [18] found doping Sn^{4+} promoted the phase transition of TiO_2 from anatase to rutile.

Previous researches have focused on the preparation of diesel oxidation catalysts by co-precipitation method, sol-gel method, and solid-phase reaction [5, 6, 15, 19, 20]. Yang et al. [19] prepared the Pt/TiO_2 catalysts via the co-precipitation method and found that the conversion of CO and C_3H_6 only reaches 50% at 232 °C. Li et al. [15] synthesized TiO_2–SnO_2 nano-composite by the sol-gel method and suggested that the conversion of TiO_2–SnO_2 to CO was 90% at 260 °C. Sharif et al. [6] prepared $Ru/[Ca_{24}Al_{28}O_{64}]^{4+}(O^{2-})_2$ through solid-state reaction and showed that the conversion of $Ru/[Ca_{24}Al_{28}O_{64}]^{4+}(O^{2-})_2$ to CO was only 82% at 240 °C due to lower dispersion of Ru. Therefore, there are critical challenges that remain in the low-temperature activity of diesel oxidation catalysts and a lot of efforts are still needed to remove CO and HCs caused in the diesel cold start. Furthermore, the current research [8, 16, 19, 21, 22] is mainly focused on the preparation of

DOC catalysts by co-precipitation and sol-gel methods, which has a small grain size, but the samples have poor crystallinity and multiple crystal phases; furthermore, the subsequent heat treatment process of mixture by co-precipitation method is required. Hydrothermal treatment is adopted in the preparation process to avoid the traditionally followed calcination processes and the formation of hard aggregation of the catalysts, which could improve low-temperature catalytic activity [23]. However, there is a lack of systematic and comprehensive studies on the one-step hydrothermal method [24, 25].

Therefore, we reported that RuO_x particles supported on the Sn^{4+}-modified TiO_2 by the one-step hydrothermal method were excellent CO and HC oxidation catalysts with promising low-temperature activity and stability. A series of $Sn_xTi_{1-x}O_2$ (x = 0, 0.33, 0.5, 0.67, 1) solid solution were prepared by the one-step hydrothermal method. $Ru/Sn_xTi_{1-x}O_2$ were then prepared by impregnation of the $Sn_xTi_{1-x}O_2$ with $RuCl_3$ to oxidize CO and C_3H_8. The effect of hydrothermal temperatures, hydrothermal time, calcination temperatures, and the molar ratios of Sn/Ti of $Ru/Sn_xTi_{1-x}O_2$ catalysts were investigated in order to improve low-temperature activity and stability.

Method
Materials
Tin (IV) chloride pentahydrate ($SnCl_4·5H_2O$) was purchased from Guangdong Kehua Stock Corporation, tetrabutyl titanate ($C_{16}H_{36}O_4Ti$) was purchased from Tianjin Kemiou Chemical Reagent Factory, and Ruthenium (III) chloride anhydrous, $RuCl_3$, (37% Ru w/w) was purchased from Aladdin.

Preparation of Catalysts
$Sn_xTi_{1-x}O_2$ solid solution was prepared by the one-step hydrothermal method. The certain amounts of $SnCl_4·5H_2O$ and $C_{16}H_{36}O_4Ti$ were dissolved in 200 mL of deionized water and 10 mL of anhydrous ethanol, respectively; then, $C_{16}H_{36}O_4Ti$ ethanol solution and $SnCl_4·5H_2O$ aqueous solution were mixed while stirring at room temperature for 0.5 h. The homogeneous mixture was put in a 250-mL autoclave at 180 °C for 24 h. After that, the mixed solution was centrifuged washing with deionized water and ethanol several times until no residues of Cl^-, and then was dried at 80 °C overnight in the oven. Subsequently, light yellow solid products were obtained, named $Sn_xTi_{1-x}O_2$. SnO_2 and TiO_2 were obtained by similar preparation methods, respectively.

$Ru/Sn_xTi_{1-x}O_2$ catalysts were prepared by impregnation of $Sn_xTi_{1-x}O_2$ with an aqueous solution including 1.0 wt.% of $RuCl_3$. These samples were ultrasonic stirred for 2 h and dried at 80 °C for 12 h, and it was then

calcined at 400 °C for 3 h (heating rate is 3 °C/min). The obtained powder was named $Ru/Sn_xTi_{1-x}O_2$.

Catalytical Performance

The activities of the catalysts were evaluated on a fixed bed quartz reactor with an electric heater. The simulative reactant gases contained a mixture of 3000 ppm CO, 600 ppm C_3H_8, 600 ppm NO, 50 ppm SO_2, 7% O_2, and N_2 balance at a gas space velocity of 60,000 mL g^{-1} h^{-1}. The gas flow rate was regulated by mass flow controllers. The temperature of fixed bed was tested by a 0.5-mm K-thermocouple which was placed in the middle of the center channels. The outlet CO and C_3H_8 were measured by a KM9106 flue gas analyzer (Kane International Limited, Britain). The conversion (X) of CO and C_3H_8 was calculated using the following equation:

$$X = \frac{c_{in} - c_{out}}{c_{in}} \times 100\%$$

where c_{in} is the initial concentration of CO or C_3H_8 and c_{out} is the instantaneous of CO or C_3H_8 at the reaction temperature; T_{50} is denoted as the low-temperature catalytic activity index.

Catalyst Characterization

X-ray diffraction (XRD) patterns of the samples were performed by power X-ray diffraction on a BRUKER D8 ADVANCE diffractometer equipped with a high-temperature chamber using Cu Kα radiation (0.15418 nm). The X-ray tube was operated at a source power of 40 kV × 40 mA.

The Brunauer-Emmett-Teller (BET) surface areas were tested by nitrogen adsorption at 77 K on a Micromeritics ASAP2020 adsorption apparatus; the specific surface area and pore distribution were calculated by the BET and BJH methods, respectively. These samples were degassed under vacuum at 300 °C for 4 h before each analysis.

Fourier transform infrared (FT-IR) spectroscopy was examined using a Nicolet is5 spectrometer at a spectral resolution of 4.0 cm^{-1}. The powders were pressed into a self-supporting wafer (about 15 mg, 12 mm diameter). The wafer was pretreated with N_2 at 300 °C for 1 h. After cooling to ambient temperature, the spectrum of samples was recorded.

Transmission electron microscopy (TEM) images of these samples were obtained by a Tecnai G2 F20 instrument at an acceleration voltage of 200 kV. The samples were ground, dispersed in ethanol, and deposited on carbon-coated copper grids prior to observation.

X-ray photoelectron spectroscopy (XPS) analysis was performed on a ESCALAB250Xi spectrometer, using monochromatic Al Kα radiation (1486.6 eV) at an accelerating power of 15 kW. The obtained sample spectra were corrected using C1s (284.6 eV) as the internal reference standard.

H_2-temperature-programmed reduction (H_2-TPR) experiments were performed in a quartz reactor connected to a thermal conductivity detector (TCD) with H_2 (6.9% vol. %)-Ar mixture (30 mL/min) as reductant. Prior to the reaction, the sample (50 mg) was pretreated in N_2 at 300 °C for 1 h and then cooled to room temperature. TPR started from room temperature to target temperature at a rate of 10 °C/min.

Temperature-programmed oxygen desorption (O_2-TPD) experiments were carried out using the same device as H_2-TPR. The spent catalyst (50 mg) was pretreated at 300 °C for 1 h under flowing Ar at 30 mL/min. Then, oxygen adsorption was conducted under an O_2–Ar mixture (20% O_2 vol. %) at 500 °C for 0.5 h. After cooling to room temperature, the system was purged in Ar (30 mL/min) for 1 h. After the treatment, the temperature was raised to target temperature (10 °C/min).

In situ infrared spectroscopy (IR) of CO adsorption was collected on a Nicolet 5700 FT-IR spectrometer at a spectral resolution of 4.0 cm^{-1}. CO adsorption was performed by exposing a self-supporting wafer of catalyst (about 15 mg) and mounted in a commercial controlled environment chamber (HTC-3). The samples were exposed to a controlled stream of CO–Ar (10% of CO by volume) at a rate of 5.0 mL/min for 40 min. The spectra were recorded at various target temperatures at a rate of 10 °C/min from room temperature to 300 °C.

Results and Discussion
Catalytic Activity and Stability

Figure 1 shows the catalytic activities of CO and C_3H_8 oxidation on the $Ru/Sn_xTi_{1-x}O_2$ catalysts under the optimal preparation conditions (Fig. S1, S2 and S3) of hydrothermal temperature at 180 °C, hydrothermal time at 24 h, and calcination temperature at 400 °C. It can be seen that catalytic performances of $Ru/Sn_xTi_{1-x}O_2$ catalysts increased firstly and then tended to be stabilized with the increase of reaction temperature. When the molar ratio of Sn/Ti is 2/1, the T_{50} of $Ru/Sn_{0.67}Ti_{0.33}O_2$ to oxidize CO and C_3H_8 is 180 °C and 320 °C, respectively, which is lower reaction temperature than other Sn/Ti molar ratios. The conversion of CO reached 90% at 240 °C, and the complete conversion of C_3H_8 could be achieved at 500 °C on the $Ru/Sn_{0.67}Ti_{0.33}O_2$ catalyst. The catalytic performance for each sample was normalized with respect to the Ru atoms on the surface and expressed in terms of turnover frequency (TOF), as shown in Fig. 2. The TOF value for $Ru/Sn_{0.67}Ti_{0.33}O_2$ was the highest among all the samples at any reaction temperature. It is attributed to the highly dispersed Ru on the surface of $Sn_{0.67}Ti_{0.33}O_2$, and the active component Ru has a strong interaction with the carrier
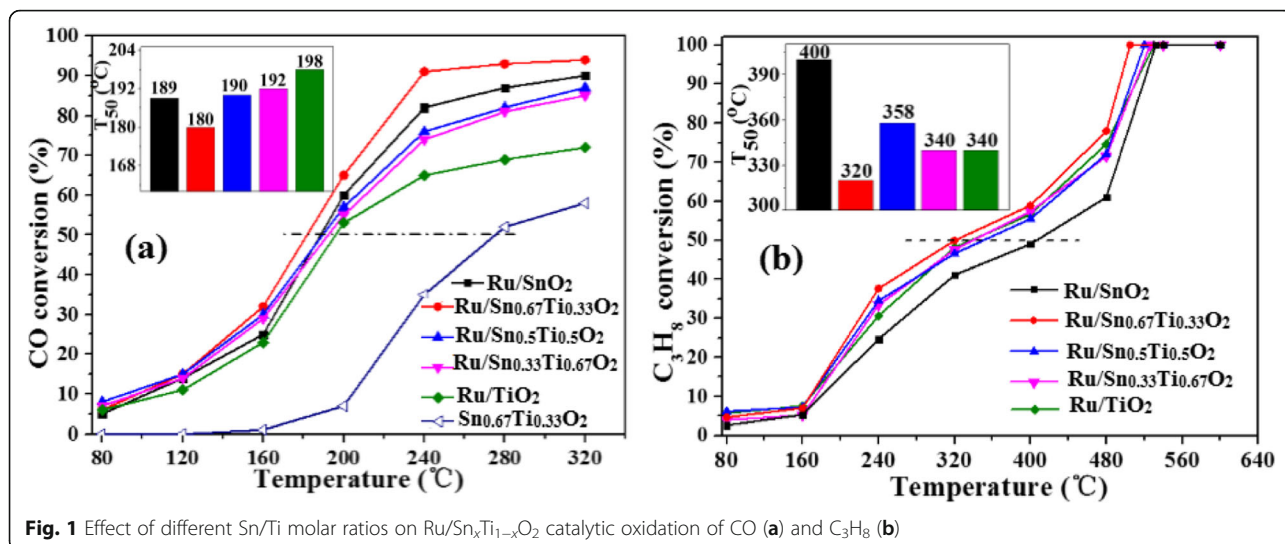
Fig. 1 Effect of different Sn/Ti molar ratios on Ru/Sn$_x$Ti$_{1-x}$O$_2$ catalytic oxidation of CO (**a**) and C$_3$H$_8$ (**b**)

Sn$_{0.67}$Ti$_{0.33}$O$_2$ [22, 26]. Sharif et al. [6] reported that the conversion of Ru/[Ca$_{24}$Al$_{28}$O$_{64}$]$^{4+}$(O^{2-})$_2$ to CO was only 82% at 240 °C. Murayama et al. [27] reported that the conversion of Au/Nb$_2$O$_5$ and Au/SiO$_2$ to CO was 55% and 38%, respectively, at 250 °C. Compared with other literatures [27, 28], when the molar ratio of Sn/Ti is 2/1, higher CO conversion can be achieved at lower temperature in this study. Okal et al. [29] reported that the T_{50} of CH$_4$ oxidized by Ru/ZnAl$_2$O$_4$ catalysts was 480, 500, and 540 °C, when the loading of Ru was 0.5 wt.%, 1.0 wt.%, and 4.5 wt.%, respectively. Wilburn et al. [30] reported that the T_{50} of CH$_4$ oxidation over 0.3Pd–0.7Pt/γ–Al$_2$O$_3$ catalyst was 360 °C. The catalytic activities of different catalysts for CO and C$_3$H$_8$ oxidation are shown in Table S1 and Table S2. Complete transformation of C$_3$H$_8$ can be achieved at a lower temperature in this work. The optimum molar ratio of Sn/Ti is 2/1,

which is consistent with the activity of CO. From the above analysis, it can be concluded that the conversion of CO and C$_3$H$_8$ is greatly affected by the molar ratio of Sn/Ti. When the molar ratio of Sn/Ti is 2/1, the T_{50} of Ru/Sn$_{0.67}$Ti$_{0.33}$O$_2$ to CO and C$_3$H$_8$ is 180 °C and 320 °C, respectively. When the reaction temperature is 240 °C, the conversion of CO can reach 90% and the complete conversion of C$_3$H$_8$ can be achieved when the reaction temperature is 500 °C.

The stability of CO and C$_3$H$_8$ was investigated in Fig. 3, under hydrothermal temperature at 180 °C, hydrothermal time at 24 h, and calcination temperature at 400 °C (Fig. S1, S2 and S3). The conversion of CO reached 90% at 240 °C, and the complete conversion of C$_3$H$_8$ could be achieved at 500 °C. Interestingly, Ru/Sn$_{0.67}$Ti$_{0.33}$O$_2$ catalyst is basically inactivated after a 12 h catalytic reaction; however, the activity of Ru/TiO$_2$ and Ru/SnO$_2$ catalysts
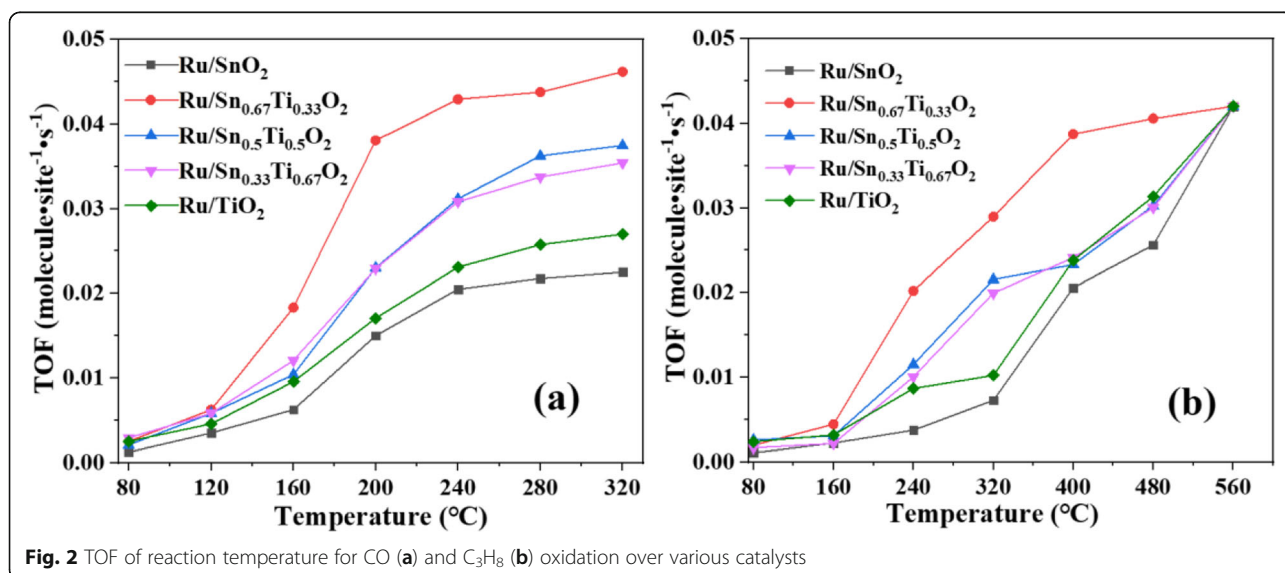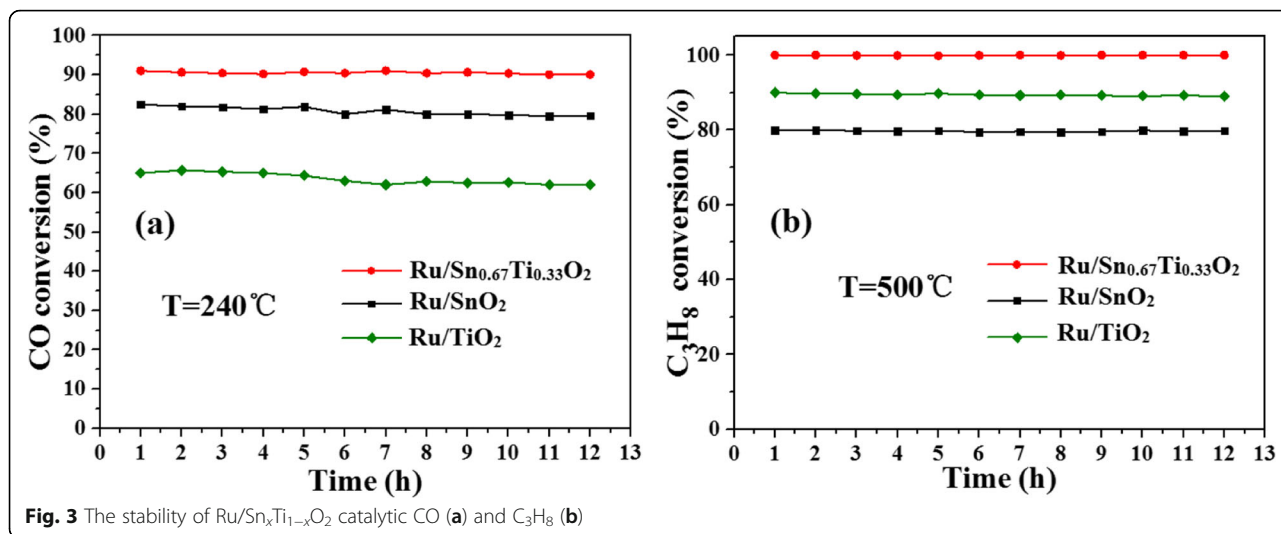

Fig. 2 TOF of reaction temperature for CO (**a**) and C$_3$H$_8$ (**b**) oxidation over various catalysts

Fig. 3 The stability of Ru/$Sn_xTi_{1-x}O_2$ catalytic CO (**a**) and C_3H_8 (**b**)

decreased slightly with the increase of time when they oxidized CO. The phenomenon indicates that the formation of $Sn_xTi_{1-x}O_2$ solid solution can not only improve the activity of the catalysts, but also increase the stability. It is attributed that Ru is highly dispersed on the surface of $Sn_{0.67}Ti_{0.33}O_2$; there is a strong interaction between the active component Ru and the carrier $Sn_{0.67}Ti_{0.33}O_2$ [26].

Catalyst Characterization
Texture Properties of $Sn_xTi_{1-x}O_2$ Supports and Ru/$Sn_xTi_{1-x}O_2$ Catalysts

Figure 4 shows the XRD patterns of both $Sn_xTi_{1-x}O_2$ solid solution and Ru/$Sn_xTi_{1-x}O_2$ catalysts. Typical peaks of anatase structure are observed in the TiO_2 (25.78°) and Ru/TiO_2 (25.67°) samples with grain sizes of about 4 nm and 5.5 nm (Table 1), respectively. A phase
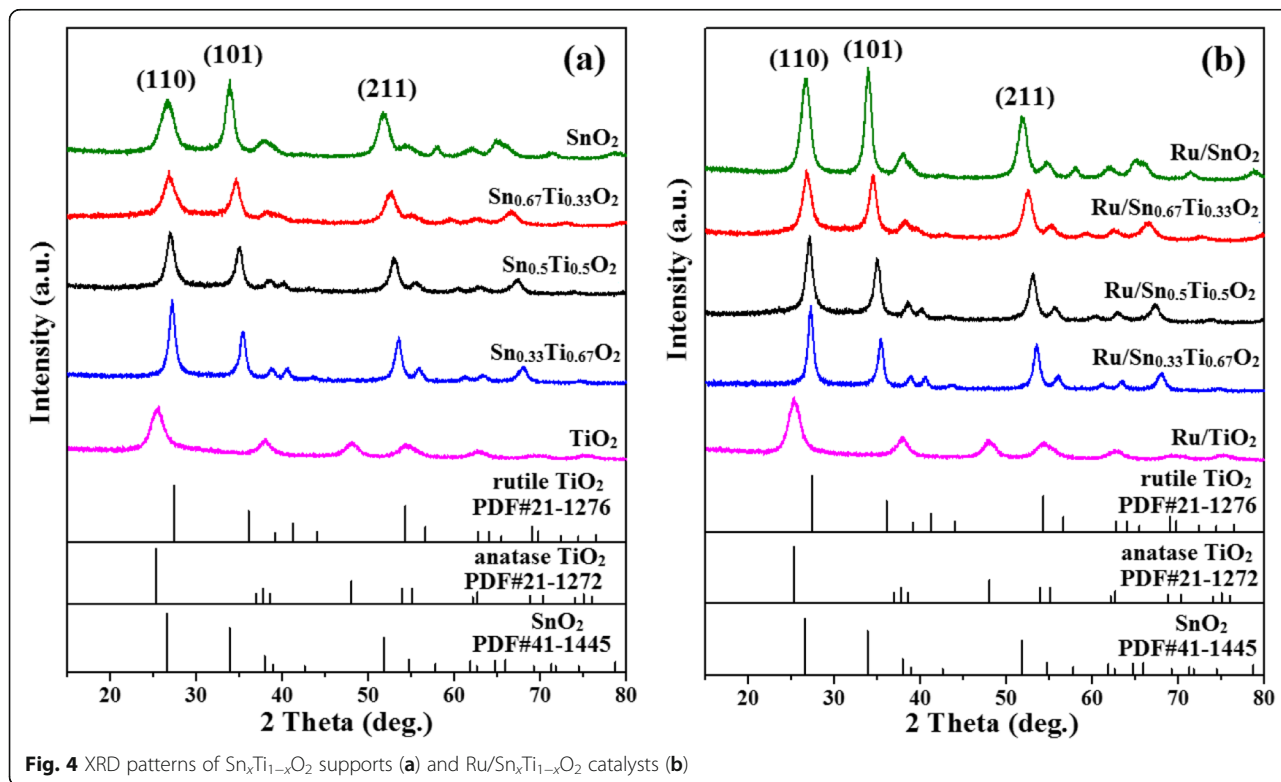

Fig. 4 XRD patterns of $Sn_xTi_{1-x}O_2$ supports (**a**) and Ru/$Sn_xTi_{1-x}O_2$ catalysts (**b**)

Fan *et al. Nanoscale Research Letters* (2020) 15:109

Page 6 of 15

Table 1 Texture properties of $Sn_xTi_{1-x}O_2$ supports and $Ru/Sn_xTi_{1-x}O_2$ catalysts

Samples	Crystalline size (nm)	Lattice parameter $a = b$, c (nm)	BET surface area ($m^2\ g^{-1}$)	$Vp/cm^3\ g^{-1}$	d_p/A
SnO_2	6	$a = 4.738$, $c = 3.187$	126.4	0.14	4.0
$Sn_{0.67}Ti_{0.33}O_2$	4.5	$a = 4.680$, $c = 3.095$	156.5	0.17	3.9
$Sn_{0.5}Ti_{0.5}O_2$	5	$a = 4.666$, $c = 3.073$	126.2	0.18	5.0
$Sn_{0.33}Ti_{0.67}O_2$	5.4	$a = 4.637$, $c = 3.027$	108.1	0.20	6.5
TiO_2	4	$a = 3.784$, $c = 2.959$	257.4	0.21	3.5
Ru/SnO_2	23	$a = 4.738$, $c = 3.187$	77.34	0.14	6.1
$Ru/Sn_{0.67}Ti_{0.33}O_2$	7.6	$a = 4.709$, $c = 3.141$	83.3	0.15	5.3
$Ru/Sn_{0.5}Ti_{0.5}O_2$	9.5	$a = 4.666$, $c = 3.073$	75.3	0.15	5.6
$Ru/Sn_{0.33}Ti_{0.67}O_2$	11	$a = 4.643$, $c = 3.044$	68.6	0.16	6.5
Ru/TiO_2	5.5	$a = 3.785$, $c = 2.961$	177.10	0.23	5.3

transition from anatase to rutile appeared with the introduction of Sn. The Ru diffraction peaks are not observed, indicating that Ru is highly dispersed on $Sn_xTi_{1-x}O_2$ surface or beyond the XRD detection limitation [31]. Furthermore, the diffraction peaks of $Sn_xTi_{1-x}O_2$ and $Ru/Sn_xTi_{1-x}O_2$ move gradually to lower angles with increasing Sn content, suggesting that the interplanar spacing d increases according to the Bragg equation, $2d \sin\theta = n\lambda$. This is consistent with the increase in tetragonal lattice parameters (a and c) in Table 1, which is attributed to the substitution of larger ionic radius Sn^{4+} (0.071 nm) for Ti^{4+} (0.068 nm). The results suggest the Sn^{4+} has been successfully doped into the TiO_2 lattice to form a uniform ($-Sn^{4+}-O-Ti^{4+}-$) solid solution while maintaining the rutile phase structure, which is in agreement with some previous studies [5, 18].

To determine the texture properties of samples, the N_2 adsorption-desorption technique was used. The N_2 adsorption-desorption isotherms and corresponding pore diameter distribution curves of these samples are shown in Fig. 5. The N_2 adsorption-desorption isotherms of SnO_2 distinctly belong to type II; others are classical type IV according to IUPAC classification and present a H2 complex hysteresis loop in a p/p_0 range of 0.4–0.95, which is a common feature of mesoporous material (Fig. 5a, c) [17, 32]. The existence of these mesopores is an important reason for the large specific surface area of catalysts [33]. All of $Sn_xTi_{1-x}O_2$ supports and $Ru/Sn_xTi_{1-x}O_2$ catalysts exhibited a narrow distribution of small-sized pores (3–8 nm), especially the $Sn_{0.67}Ti_{0.33}O_2$ support and $Ru/Sn_{0.67}Ti_{0.33}O_2$ catalysts, with the pore diameter mainly uniformly distributed around 5 nm (Fig. 5b, d). This phenomenon suggested that an appropriate amount of Sn can weaken the diffusion coefficient of the catalytic surface and indirectly hinder the agglomeration of the crystallites [17].
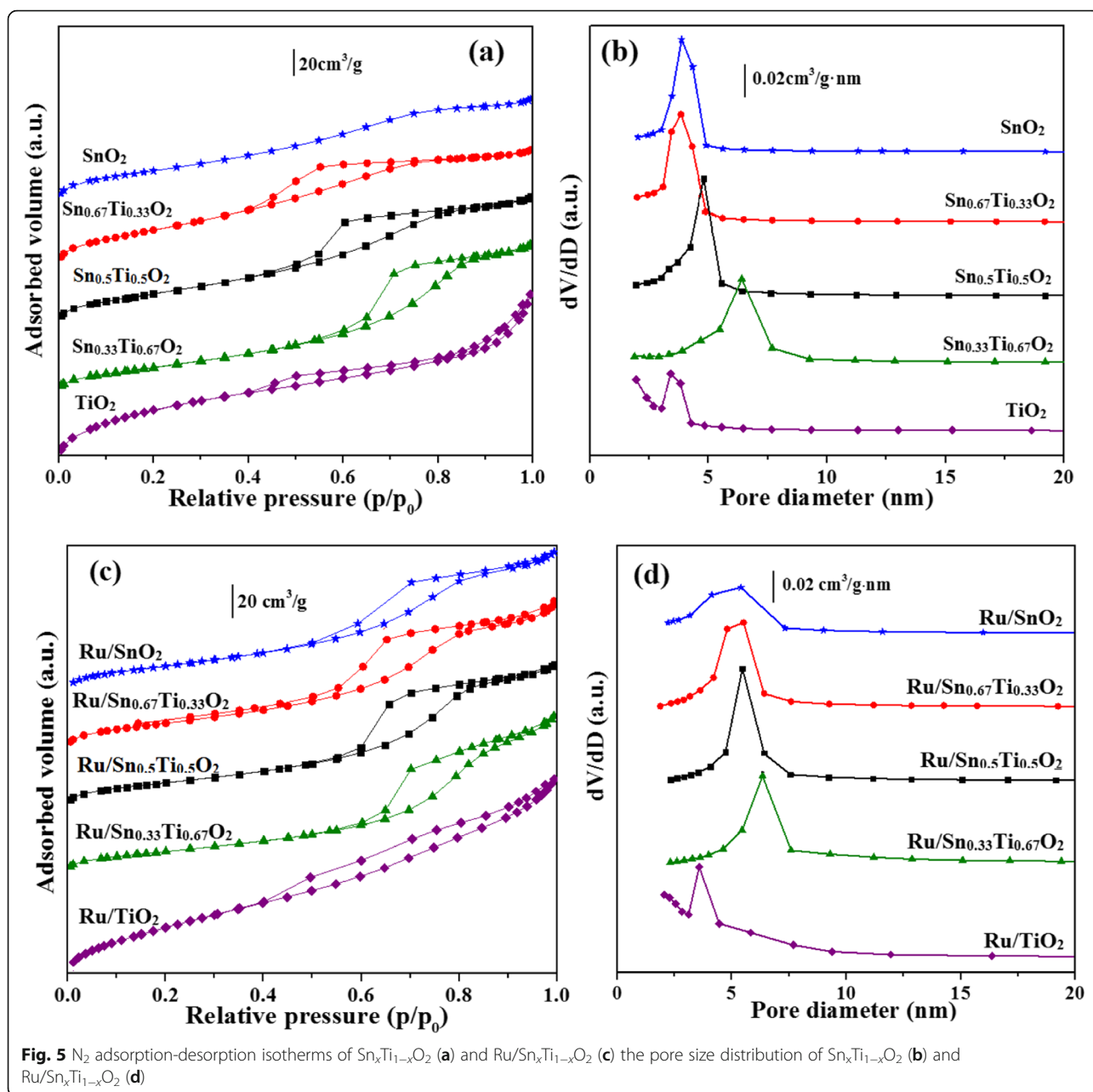
The texture properties of $Sn_xTi_{1-x}O_2$ supports and $Ru/Sn_xTi_{1-x}O_2$ catalysts are listed in Table 1. The specific surface area and pore distribution were calculated by the BET and BJH method. Both the specific surface area and pore volume of $Sn_{0.67}Ti_{0.33}O_2$ are 156.5 $m^2\ g^{-1}$ and 0.17 $cm^3\ g^{-1}$, respectively. But both specific surface area and pore volume of the $Ru/Sn_{0.67}Ti_{0.33}O_2$ catalyst are decreased compared with the $Sn_{0.67}Ti_{0.33}O_2$ support, which indicates that Ru loaded on the $Sn_{0.67}Ti_{0.33}O_2$ surface. Moreover, the $Ru/Sn_{0.67}Ti_{0.33}O_2$ catalyst is sintered and the open pore structure collapsed to form plugged pores during the high-temperature calcination process [31]. Nevertheless, $Ru/Sn_{0.67}Ti_{0.33}O_2$ still maintains larger specific surface area (83.3 $m^2\ g^{-1}$) and smaller pore diameter (5.3 nm) in comparison with other rutile samples such as $Ru/Sn_{0.33}Ti_{0.67}O_2$, $Ru/Sn_{0.5}Ti_{0.5}O_2$, and Ru/SnO_2.

Figure 6 shows the FT-IR spectra of $Sn_xTi_{1-x}O_2$ supports and $Ru/Sn_xTi_{1-x}O_2$ catalysts. All the samples present similar vibration peaks at analogous wavenumber positions. The adsorption at around 3223.68 cm^{-1} is due to surface hydroxyl groups neighboring oxygen vacancy sites [34, 35]. The bands of 1501.86–1618.18 cm^{-1} belong to the angular vibration peak of water. The symmetrical stretching vibration peak of lattice oxygen appears at 1028.17 cm^{-1}. The band of 527.27–681.2 cm^{-1} may be attributed to the stretching vibration peak of TiO_2 or SnO_2 [34]. Compared with $Sn_xTi_{1-x}O_2$ supports, $Ru/Sn_xTi_{1-x}O_2$ spectrum broadens, indicating that the active component Ru and support $Sn_xTi_{1-x}O_2$ have some interaction, resulting in the surface defects of catalysts [36, 37].

Morphology of Catalysts

Low- and high-resolution TEM, HRTEM images, and the particle size distribution of $Ru/Sn_xTi_{1-x}O_2$ are exhibited in Fig. 7. Based on the observation of the TEM images presented in Fig. 7a, d, g, j, and m, we find that all samples are composed of well-defined particles with irregular shapes and disordered mesoporous structure, which is formed by the agglomeration of the nanoparticles [38]. Furthermore, it can be seen that the Ru/

Fig. 5 N_2 adsorption-desorption isotherms of $Sn_xTi_{1-x}O_2$ (**a**) and $Ru/Sn_xTi_{1-x}O_2$ (**c**) the pore size distribution of $Sn_xTi_{1-x}O_2$ (**b**) and $Ru/Sn_xTi_{1-x}O_2$ (**d**)

$Sn_{0.67}Ti_{0.33}O_2$ sample has the highest degree of agglomeration because of the smallest grain size among these samples. From the HRTEM images (Fig. 7b, e, h, k, n), there is only one kind of lattice fringes with 0.327 nm, which is compatible with (110) plane of these samples. Besides, we find that the lattice fringes of TiO_2 and SnO_2 are not observed, which is attributed to Sn^{4+} having been successfully doped into the lattice of TiO_2 to form a homogeneous $Sn_xTi_{1-x}O_2$ solid solution [39]. The results are consistent with XRD. The Ru particle size distribution (Fig. 7c, f, i, l, o) shows that the approximate sizes of Ru particles ranged from 3 to 20 nm. The introduction of Sn^{4+} could effectively decrease the

sizes of Ru particles and achieve a higher dispersion on the $Sn_xTi_{1-x}O_2$ surface. Comparing with other samples, the Ru particle size distribution of $Ru/Sn_{0.5}Ti_{0.5}O_2$ sample was wider (< 13 nm), which may be caused by the interaction between ($-Sn^{4+}-O-Ti^{4+}-$) species and Ru [26]. The $Ru/Sn_{0.67}Ti_{0.33}O_2$ catalyst has better Ru dispersion and smaller particle size (5.49 nm) among all samples.

Surface Properties of Catalysts

To further determine the elementary states and surface composition, XPS analysis was carried out. Figure 8 shows the XPS spectra of Sn 3d, Ti 2p, O 1s, and Ru 3d
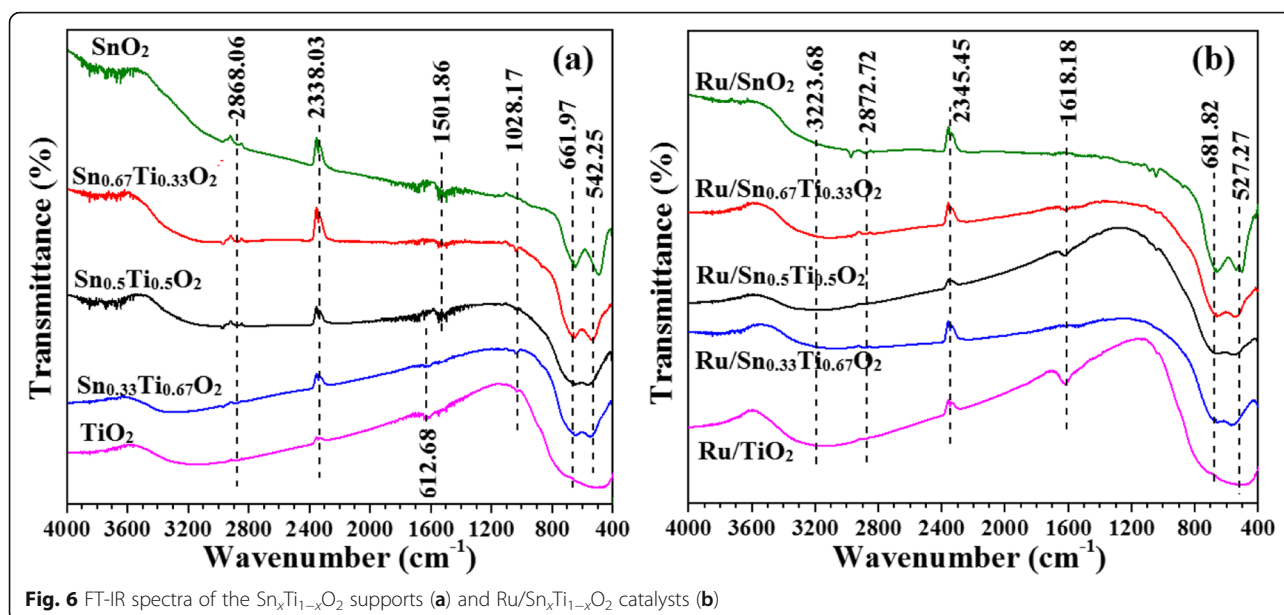
Fig. 6 FT-IR spectra of the $Sn_xTi_{1-x}O_2$ supports (**a**) and $Ru/Sn_xTi_{1-x}O_2$ catalysts (**b**)

for the $Sn_xTi_{1-x}O_2$ supports and $Ru/Sn_xTi_{1-x}O_2$ catalysts. The XPS binding energy values of the Sn $3d_{3/2}$ and Sn $3d_{5/2}$ are observed at 486.6–487.5 eV and 494.9–496.1 eV, respectively, which are characteristic of Sn^{4+} species in $Sn_xTi_{1-x}O_2$ supports or $Ru/Sn_xTi_{1-x}O_2$ catalysts. Interestingly, the binding energy of Sn $3d_{3/2}$ and Sn $3d_{5/2}$ shifted to higher values after the introduction of Sn^{4+}, indicating some of the Sn^{4+} replace the Ti^{4+} sites and have a strong interaction with TiO_2, which is in agreement with XRD. Also, the oxyen vacancies may be created by the lower valent $Sn^{\delta+}$ [5]. Two peaks corresponding to Ti $2p_{3/2}$ and Ti $2p_{1/2}$ are observed at 458.7–459.9 eV and 464.3–465.8 eV in the XPS spectra of Ti 2p, suggesting that Ti^{4+} and Ti^{3+} existed in the samples, and the binding energy values of Ti $2p_{3/2}$ and Ti $2p_{1/2}$ shifted to higher binding energy values with the increase of Sn^{4+}, further proving the existence of oxygen vacancies. It can be seen from Table 3 that the Sn/Ti molar ratio by XPS is observed to be slightly higher than theoretical calculation, indicating that Sn is enriched on the surface of catalysts, which leads to more oxygen vacancies. Because the electronegativity of Sn (1.96) is larger than that of Ti (1.62), in other words, the electron-capturing ability of Sn is stronger than that of Ti, which causes the redox equilibrium ($Sn^{4+}+Ti^{3+} \rightarrow Sn^{\delta+}+Ti^{4+}$) shifting to right [32].

The high-resolution spectra of the O 1s ionization feature are numerically consistent with the Gaussian feature and deconvoluted into two peaks [5]. Higher binding energy (O', 532.1 eV) is caused by chemisorbed oxygen that formed the (O_2^-, O^-, or O_2^{2-}) species. However, the O" (529.9 eV) is the characteristic peak of O^{2-} on the surface of metal oxides. Interestingly, the binding

energy of O 1s shifted to higher values after the addition of Sn^{4+}.

Ru 3d spectra present Ru^{4+} and lower value $Ru^{\delta+}$. The signal of Ru $3d_{5/2}$ is often used to analyze the charge state of the Ru species, since another Ru $3d_{3/2}$ overlaps with C 1s at around 284.0 eV [40]. The binding energy of 282.0–283.5 eV is assigned to Ru $3d_{5/2}$, which corresponded to Ru^{4+}. The lower binding energy at around 280.2–281.7 eV is attributed to lower state $Ru^{\delta+}$, and the $Ru^{\delta+}$ relative ratio in $Ru/Sn_{0.67}Ti_{0.33}O_2$ reaches 53.9%, which is higher than other catalysts. It could be explained that the strong interaction between $Sn_{0.67}Ti_{0.33}O_2$ and Ru caused a larger amount of surface reactive oxygen species [26].

XPS and EDS analyses are performed to determine the surface and bulk composition of the samples as shown in Table 2. Surface and bulk Ru analysis shows that $Ru/Sn_{0.67}Ti_{0.33}O_2$ has the highest surface Ru (0.69 wt.%) and bulk Ru (0.40 wt.%) among all the catalysts, indicating that the active component Ru is more evenly distributed on the $Sn_{0.67}Ti_{0.33}O_2$ support, and more Ru species enters the internal of $Sn_{0.67}Ti_{0.33}O_2$ to form a strong interaction.

In order to further investigate the reduction performance of the $Ru/Sn_xTi_{1-x}O_2$ catalysts, temperature-programmed reduction studies are performed (Fig. 9). The shapes of these H_2-TPR profiles are almost identical. The reduction peaks of $Ru/Sn_xTi_{1-x}O_2$ are divided into two parts: the low-temperature reduction peaks 80–270 °C are associated to the lower state $Ru^{\delta+}$ reduced from RuO_2 and a significant amount of Sn^{4+} which could be reduced to lower valent $Sn^{\delta+}$ or can be attributed to the reduction of surface oxygen [41], while the high-temperature reduction peaks 600–640 °C are
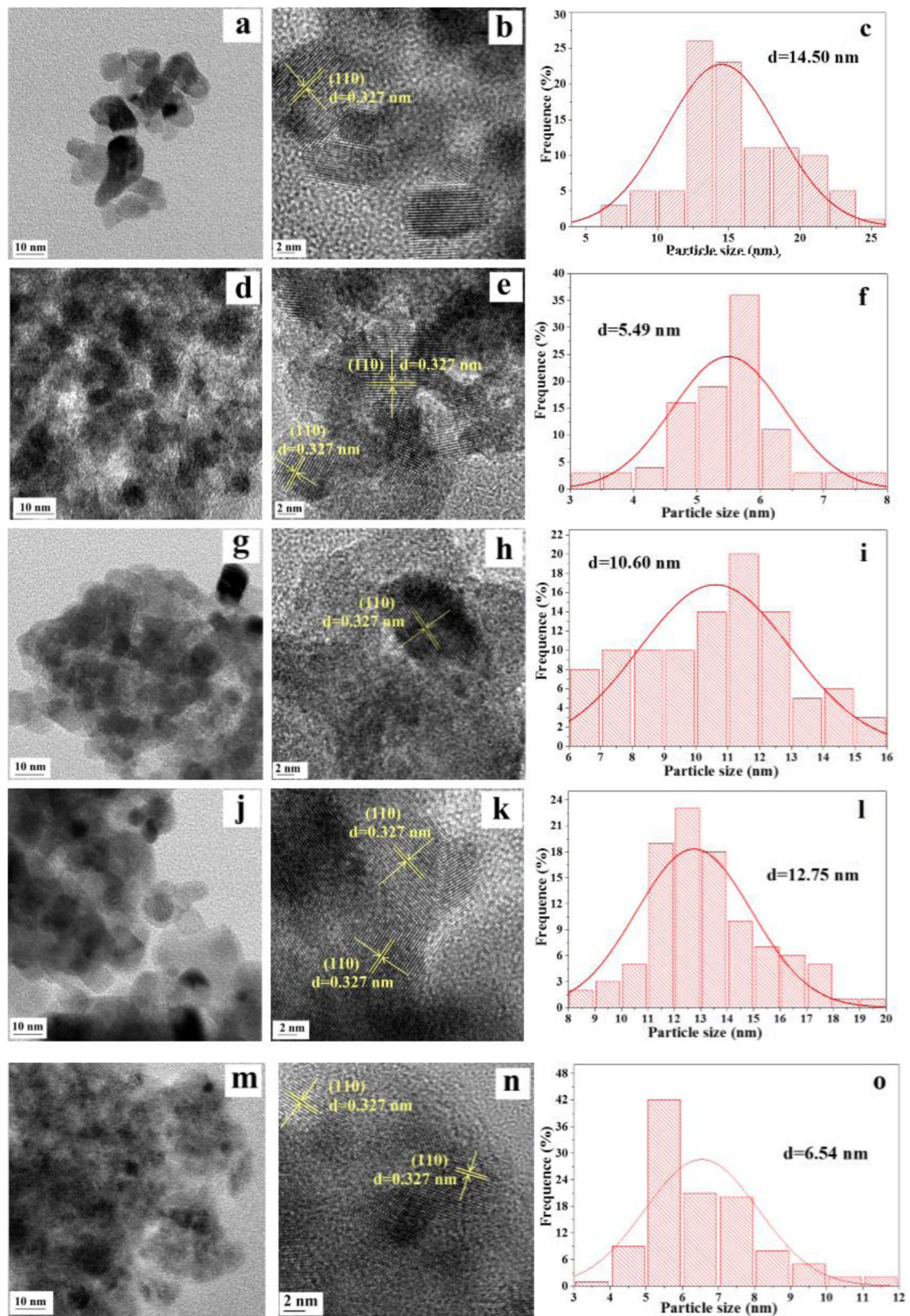
Fig. 7 TEM, HRTEM images, and the particle size distribution of **a**, **b**, **c** Ru/SnO$_2$; **d**, **e**, **f** Ru/Sn$_{0.67}$Ti$_{0.33}$O$_2$; **g**, **h**, **i** Ru/Sn$_{0.5}$Ti$_{0.5}$O$_2$; **j**, **k**, **l** Ru/Sn$_{0.33}$Ti$_{0.67}$O$_2$; and **m**, **n**, **o** Ru/TiO$_2$
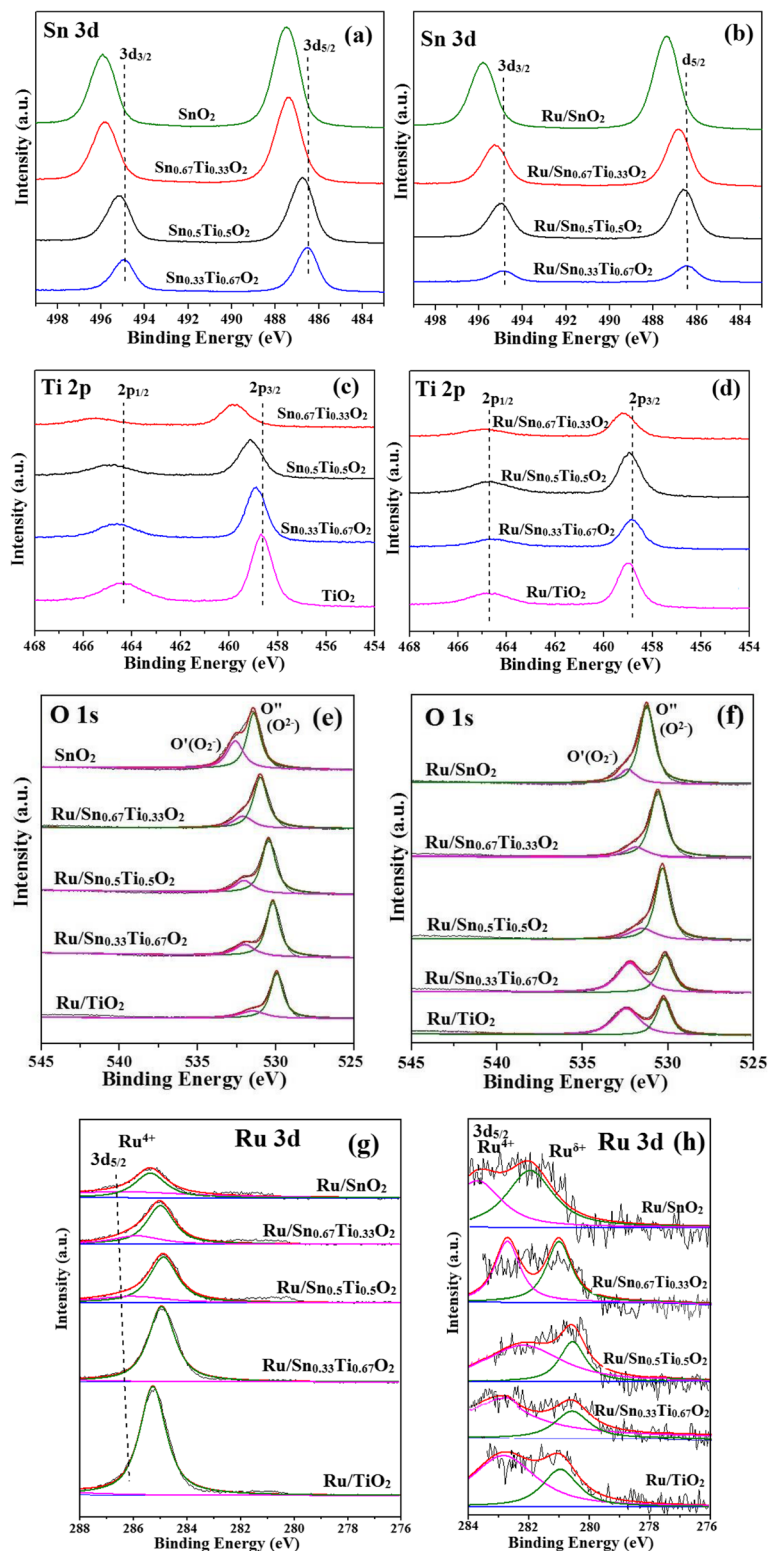
Fig. 8 XPS spectra (Sn3d (**a**, **b**), Ti2p (**c**, **d**), O1s (**e**, **f**) and Ru3d (**g**, **h**)) of $Sn_xTi_{1-x}O_2$ supports and $Ru/Sn_xTi_{1-x}O_2$ catalysts

Fan *et al. Nanoscale Research Letters*   (2020) 15:109

Page 11 of 15

Table 2 The surface compositions by XPS and bulk compositions by EDS of the $Sn_xTi_{1−x}O_2$ supports and $Ru/Sn_xTi_{1−x}O_2$ catalysts

Samples	C 1s	O 1s	Ti 2p	Sn 3d	Sn/Ti	Ru (XPS)	Ru (EDS)
SnO_2	21.4	62.06	0	16.90			
$Sn_{0.67}Ti_{0.33}O_2$	31.23	48.35	5.98	14.44	2.41		
$Sn_{0.5}Ti_{0.5}O_2$	22.51	56.16	9.57	11.75	1.23		
$Sn_{0.33}Ti_{0.67}O_2$	23.41	55.70	13.20	7.69	0.58		
TiO_2	36.59	44.00	19.41	0	0		
Ru/SnO_2	16.35	58.58	0	24.94		0.37	0.20
$Ru/Sn_{0.67}Ti_{0.33}O_2$	22.95	53.58	7.66	15.62	2.04	0.69	0.40
$Ru/Sn_{0.5}Ti_{0.5}O_2$	22.4	53.82	11.33	12.27	1.08	0.64	0.28
$Ru/Sn_{0.33}Ti_{0.67}O_2$	29.88	56.95	8.33	4.56	0.55	0.41	0.26
Ru/TiO_2	37.23	50.89	11.50	0	0	0.38	0.24

Table 3 Hydrogen consumption of $Ru/Sn_xTi_{1−x}O_2$ catalysts

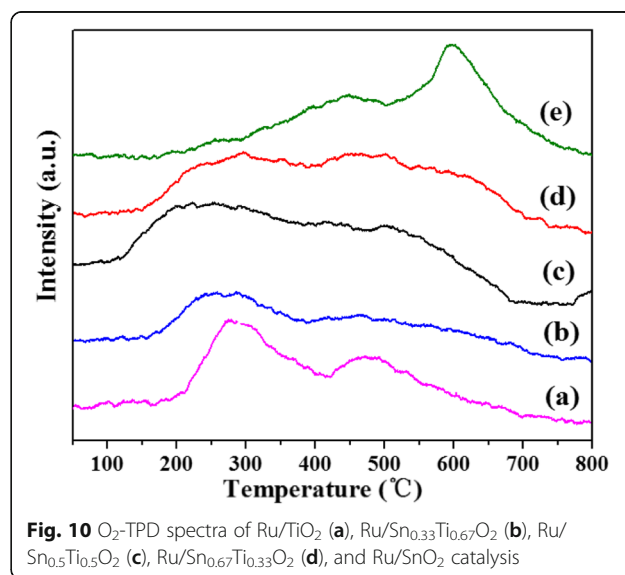| Samples	Total H_2 consumption (μmol/g)	H_2 consumption at 80–270 °C (μmol/g)	H_2 consumption at 400–640 °C (μmol/g)
Ru/SnO_2	11694.59	854.18	10840.41
$Ru/Sn_{0.67}Ti_{0.33}O_2$	8273.80	749.44	7524.36
$Ru/Sn_{0.5}Ti_{0.5}O_2$	7001.22	563.05	6438.17
$Ru/Sn_{0.33}Ti_{0.67}O_2$	5699.90	432.77	5267.13
Ru/TiO_2	474.80	396.63	78.17

associated to Sn^0 reduced from $Sn^{\delta+}$ or the reduction of bulk oxygen of catalysts [26, 42], which is consistent with XPS results. The reduction temperature of $Ru/Sn_xTi_{1−x}O_2$ moves towards lower temperature, peaks broaden and H_2 consumption increase with the addition of Sn, and hydrogen consumption from the H_2-TPR measurements are shown in Table 3. The dispersion of active components on the surface of the samples has a significant effect on the reduction of surface oxygen, and hydrogen could be more easily activated with higher dispersion of Pd, resulting in the increase of H_2 consumption [43]. Therefore, we can infer that the introduction of Sn significantly increased the dispersion of Ru on the carrier, which may have resulted from the formation of $Sn_xTi_{1−x}O_2$ solid solution. The results are in good agreement with XRD and

TEM. Because the reduction of TiO_2 is usually difficult to conduct at low temperature, there are no peaks of the TiO_2 reduction observed during the H_2-TPR from 50 to 800 °C [15]. Nevertheless, the $Ru/Sn_{0.67}Ti_{0.33}O_2$ still exhibits a higher H_2 consumption.

The O_2-TPD experiments (Fig. 10) of $Ru/Sn_xTi_{1−x}O_2$ samples are imposed to gain insight into the mobility of surface and lattice oxygen. The signal at low temperature (< 200 °C) is attracted by the desorption of surface chemisorbed oxygen ($O_2^−$, $O_2^{2−}$, or $O^−$ species); the main peak centered at 280 °C or 500 °C which is attributed to the desorption of the structure oxygen species, and the peaks above 600 °C are assignable to the desorption of the lattice oxygen ($O^{2−}$) species [44]. The incorporation of Sn increased the adsorbed oxygen species and shifted to a lower temperature [45]. The results indicate that the incorporation of Sn improved the oxygen activation ability of the $Ru/Sn_xTi_{1−x}O_2$ samples and the interaction between the carriers $Sn_xTi_{1−x}O_2$ and active component Ru [46, 47].

Fig. 9 H_2-TPR spectra of $Ru/Sn_xTi_{1−x}O_2$ catalysts

Fig. 10 O_2-TPD spectra of Ru/TiO_2 (**a**), $Ru/Sn_{0.33}Ti_{0.67}O_2$ (**b**), $Ru/Sn_{0.5}Ti_{0.5}O_2$ (**c**), $Ru/Sn_{0.67}Ti_{0.33}O_2$ (**d**), and Ru/SnO_2 catalysis
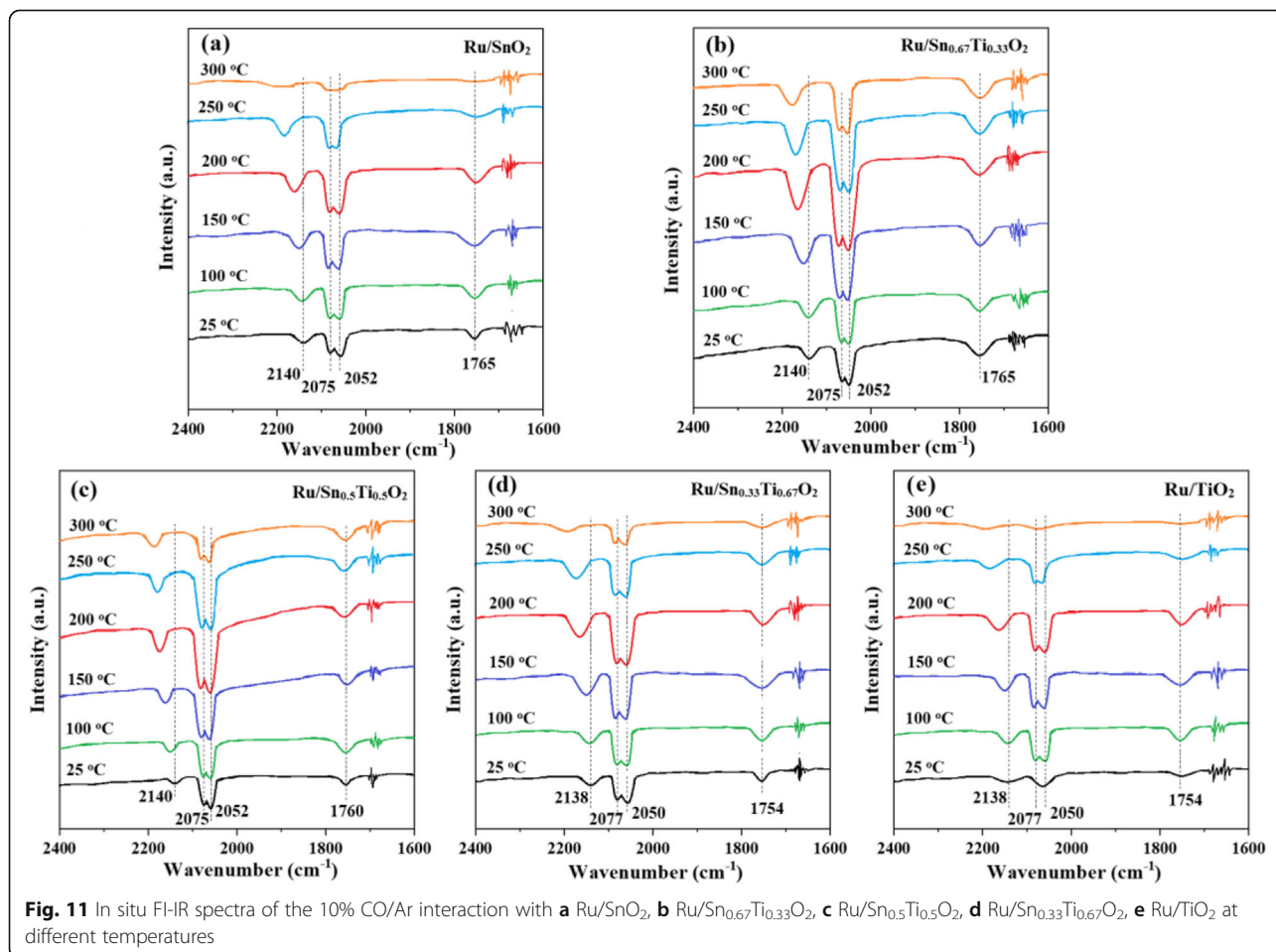
CO and/or O_2 Interaction with these Samples

The in situ FI-IR spectra of CO adsorption are recorded to further investigate the effect of the ruthenium oxide species, as shown in Fig. 11. The band located at 2052 cm^{-1} is attributed to linear CO adsorbed on reduced Ru crystallites ($Ru^{\delta+}$–CO), the band at 2140 cm^{-1} and 2075 cm^{-1} can be assigned to two different types of multicarbonyl species on partially oxidized Ru sites ($Ru^{n+}(CO)_x$), and the band at 1765 cm^{-1} is attributed to ($Sn_xTi_{1-x}O_2$)Ru–CO species [48, 49]. The $Ru^{\delta+}$–CO adsorption peaks at room temperature indicate the presence of some lower state $Ru^{\delta+}$ species. This is in agreement with the XPS results. However, the desorption temperature of the $Ru^{\delta+}$–CO peak is related to the Sn/Ti ratio and temperature. As the temperature increases, the peak intensity enhances firstly and then decreases gradually. Simultaneously, the CO adsorption peak moves to a higher wave number (2052 cm^{-1} at 25 °C and 2060 cm^{-1} at higher temperatures). This red-shift indicates that Sn^{4+} has stronger electron-donating capability [50]. For the Ru/SnO_2, Ru/$Sn_{0.5}Ti_{0.5}O_2$, Ru/$Sn_{0.33}Ti_{0.67}O_2$, and Ru/TiO_2 samples, the CO maximum adsorption peak on $Ru^{\delta+}$ appears at about 200 °C and disappears basically at 300 °C. For the Ru/$Sn_{0.67}Ti_{0.33}O_2$ sample, the CO maximum adsorption peak on $Ru^{\delta+}$ appears at about 200 °C, which can be observed clearly even at 300 °C. It can be concluded that $Ru^{\delta+}$ is much more stable in Ru/$Sn_{0.67}Ti_{0.33}O_2$ sample, which can provide more CO adsorption sites than in the other samples.

Possible Reaction Mechanism over the Ru/$Sn_xTi_{1-x}O_2$ Catalysts

According to the characterizations mentioned above, a possible reaction mechanism of CO and C_3H_8 oxidation is proposed and schematized in Fig. 12. Based on the XPS results, electrons migrate between Ru and $Sn_xTi_{1-x}O_2$ solid solution; because the electronegativity of Ru (2.22) is larger than that of Ti (1.62) and Sn (1.96), the electrons will transfer from the $Sn_xTi_{1-x}O_2$ solid solution to Ru^{4+}, in which lower state $Ru^{\delta+}$ will be generated. Meanwhile, $-Ti^{4+}-O-Sn^{4+}-$ species are oxidized and more oxygen will be absorbed on the surface of $Sn_xTi_{1-x}O_2$ solid solution, which can provide oxygen to the oxidation reaction of CO and C_3H_8. At the same time, the by-products produced in the oxidation process will also be adsorbed on the surface of $Sn_xTi_{1-x}O_2$ solid
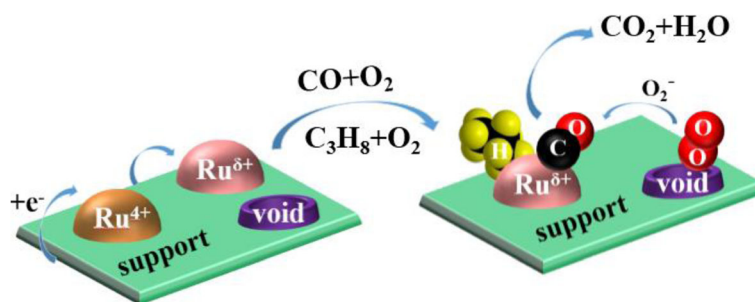

Fig. 11 In situ FI-IR spectra of the 10% CO/Ar interaction with **a** Ru/SnO_2, **b** Ru/$Sn_{0.67}Ti_{0.33}O_2$, **c** Ru/$Sn_{0.5}Ti_{0.5}O_2$, **d** Ru/$Sn_{0.33}Ti_{0.67}O_2$, **e** Ru/TiO_2 at different temperatures

Fig. 12 Possible reaction mechanism of CO and C_3H_8 over $Ru/Sn_xTi_{1-x}O_2$

solution, which will not deteriorate the activity of $Ru^{\delta+}$ species. It is also the reason for the high stability of the catalysts. Moreover, the lower state $Ru^{\delta+}$ species have more metal properties, which play a crucial role in the activation of CO and C_3H_8 [40]. Compared with Ru/TiO_2 and Ru/SnO_2, high dispersion of Ru on $Sn_xTi_{1-x}O_2$ solid solution is also an important cause for their excellent activity and stability. Based on O_2-TPD analysis, O_2 is first adsorbed on the surface of catalysts to form O_2^- species and CO and C_3H_8 adsorbed on $Ru^{\delta+}$ species react with O_2^- species to produce CO_2 and H_2O, which is a Langmuir-Hinshelwood mechanism.

Conclusions

A series of $Ru/Sn_xTi_{1-x}O_2$ catalysts were prepared by a one-step hydrothermal method for the catalytic oxidation of CO and C_3H_8. The preparation conditions of $Ru/Sn_xTi_{1-x}O_2$ catalysts were optimized for CO oxidation reaction. $Ru/Sn_{0.67}Ti_{0.33}O_2$ catalyst shows best CO catalytic activity and stability at low temperature under the condition of hydrothermal temperature at 180 °C, hydrothermal time at 24 h, and calcination temperature at 400 °C.

The effects of different molar ratios of Sn/Ti on the catalytic properties of $Ru/Sn_xTi_{1-x}O_2$ catalysts for CO and C_3H_8 were investigated under the optimum preparation conditions. The results show that the $Ru/Sn_{0.67}Ti_{0.33}O_2$ catalyst exhibits better low-temperature activity and stability. The conversion of CO reached 90% at 240 °C, and T_{50} of which keeps at 180 °C. The complete conversion of C_3H_8 could be achieved at 500 °C, and its T_{50} remains at 320 °C. The excellent catalytic activity of $Ru/Sn_{0.67}Ti_{0.33}O_2$ catalyst is attributed to the factors listed as follows.

(1) The successful incorporation of Sn^{4+} into the TiO_2 lattice to replace Ti^{4+} forms a homogeneous solid solution ($-Sn^{4+}-O-Ti^{4+}-$ species), which enhances the interaction between active component Ru and carrier $Sn_xTi_{1-x}O_2$. The crystal growth of the anatase phase can be inhibited by the introduction

of Sn^{4+}, which results in the presence of the rutile phase.

(2) Ultrafine Ru nanoparticles (~ 5 nm) are highly dispersed on $Sn_xTi_{1-x}O_2$ support, suggesting that the introduction of Sn^{4+} could not only prevent grain agglomeration and induce a smaller grain size, but also produce more defects such as oxygen vacancies.

(3) CO and C_3H_8 species can be absorbed on $Ru^{\delta+}$ sites; O_2^- is formed by the adsorption of O_2 on the oxygen vacancies. The adsorbed CO and C_3H_8 react with O_2^- to produce CO_2 and H_2O.

Supplementary information

Additional file 1: Figure S1 Effect of different hydrothermal temperature on $Ru/Sn_{0.67}Ti_{0.33}O_2$ catalytic CO. **Figure S2** Effect of different hydrothermal time on $Ru/Sn_{0.67}Ti_{0.33}O_2$ catalytic CO. **Figure S3** Effect of different calcination temperature on $Ru/Sn_{0.67}Ti_{0.33}O_2$ catalytic CO. **Table S1** Catalytic activity comparison of different catalysts for CO oxidation. **Table S2** Catalytic activity comparison of different catalysts for C_3H_8 oxidation

Fan *et al. Nanoscale Research Letters*   (2020) 15:109

Page 14 of 15

Availability of Data and Materials

Competing Interests

References

1. Shukla PC, Gupta T, Labhasetwar NK, Khobaragade R, Gupta NK, Agarwal AK (2017) Effectiveness of non-noble metal based diesel oxidation catalysts on particle number emissions from diesel and biodiesel exhaust. Sci Total Environ 574:1512–1520
2. Granger P (2017) Challenges and breakthroughs in post-combustion catalysis: how to match future stringent regulations. Catal Sci Technol. 7: 5195–5211
3. Wu QH, Gao W, He H (2006) Study SO_2 effect on the selective catalytic reduction of NO_x with propene over ag/Al$_2$O$_3$ by in situ DRIFTS. Chin J Catal 27:403–407
4. Yang ZZ, Zhang N, Cao Y, Li YX, Liao YW, Li YP, Gong MC, Chen YQ (2017) Promotional effect of lanthana on the high-temperature thermal stability of Pt/TiO$_2$ sulfur-resistant diesel oxidation catalysts. RSC Adv 7:19318–19329
5. Dong LH, Tang YX, Li B, Zhou LY, Gong FZ, He HX, Sun BZ, Tang CJ, Gao F, Dong L (2016) Influence of molar ratio and calcination temperature on the properties of Ti$_x$Sn$_{1-x}$O$_2$ supporting copper oxide for CO oxidation. Appl Catal B 180:451–462
6. Sharif MJ, Kitano M, Inoue Y, Niwa Y, Abe H, Yokoyama T, Hara M, Hosono H (2015) Electron donation enhanced CO oxidation over Ru-loaded 12CaO·7Al$_2$O$_3$ electride catalyst. J Phys Chem C 119:11725–11731
7. Boucouvalas Y, Zhang ZL, Verykios XE (1996) Partial oxidation of methane to synthesis gas via the direct reaction scheme over Ru/TiO$_2$ catalyst. Catal Lett 38:189–195
8. Dai QG, Bai SX, Wang JW, Li M, Wang XY, Lu GZ (2013) The effect of TiO$_2$ doping on catalytic performances of Ru/CeO$_2$ catalysts during catalytic combustion of chlorobenzene. Appl Catal B 142-143:222–233
9. Di L, Wu GJ, Dai WL, Guan NJ, Li LD (2015) Ru/TiO$_2$ for the preferential oxidation of CO in H$_2$-rich stream: effects of catalyst pre-treatments and reconstruction of Ru sites. Fuel 143:318–326
10. Zen JM, Kumar AS, Chen JC (2001) Electrochemical behavior of lead–ruthenium oxide pyrochlore catalyst: redox characteristics in comparison with that of ruthenium dioxide. J Mol Catal A 165:177–188
11. Xue LX, Meng TT, Yang W, Wang KZ (2017) Corrigendum to "recent advances in ruthenium complex-based light-driven water oxidation catalysts". J Photochem Photobiol B-Biol 168:193
12. Ftouni J, Murillo AM, Goryachev A, Hofmann JP, Hensen EJM, Lu L, Kiely CJ, Bruijnincx PCA, Weckhuysen BM (2016) ZrO$_2$ is preferred over TiO$_2$ as support for the Ru-catalyzed hydrogenation of levulinic acid to γ-valerolactone. ACS Catal 6:5462–5472
13. Seki K (2010) Development of RuO$_2$/rutile-TiO$_2$ catalyst for industrial HCl oxidation process. Catal Surv Jpn 14:168–175
14. Omotoso T, Boonyasuwat S, Crossley SP (2014) Understanding the role of TiO$_2$ crystal structure on the enhanced activity and stability of Ru/TiO$_2$ catalysts for the conversion of lignin-derived oxygenates. Green Chem 16: 645–652
15. Li KR, Wang YJ, Wang SR, Zhu BL, Zhang SM, Huang WP, Wu SH (2009) A comparative study of CuO/TiO$_2$-SnO$_2$, CuO/TiO$_2$ and CuO/SnO$_2$ catalysts for low-temperature CO oxidation. J Energy Chem 18:449–452
16. Huang J, Wang SR, Guo XZ, Wang D, Zhu BL, Wu SH (2008) The preparation and catalytic behavior of CuO/Ti$_x$Sn$_{1-x}$O$_2$ catalysts for low-temperature carbon monoxide oxidation. Catal Commun 9:2131–2135
17. Bai XX, Pan LY, Zhao P, Fan DD, Li WH (2016) A new solid acid SO_4^{2-}/TiO$_2$ catalyst modified with tin to synthesize 1,6-hexanediol diacrylate. Chin J Catal 37:1469–1476
18. Mehraza S, Konsong P, Talebd A, Dokhane N, Sikong L (2019) Large scale and facile synthesis of Sn doped TiO$_2$ aggregates using hydrothermal synthesis. Sol Energy Mater Sol Cells 189:254–262
19. Yang ZZ, Zhang N, Cao Y, Gong MC, Zhao M, Chen YQ (2014) Effect of yttria in Pt/TiO$_2$ on sulfur resistance diesel oxidation catalysts: enhancement of low-temperature activity and stability. Catal Sci Technol 4:3032–3043
20. Gu L, Chen X, Zhou Y, Zhu QL, Huang HF, Lu HF (2017) Propene and CO oxidation on Pt/Ce-Zr-SO$_4^{2-}$ diesel oxidation catalysts: effect of sulfate on activity and stability. Chin J Catal 38:607–615
21. Miceli P, Bensaid S, Russo B, Fino D (2014) CeO$_2$-based catalysts with engineered morphologies for soot oxidation to enhance soot-catalyst contact. Nanoscale res. Lett. 9 (1): 254.
22. Zhang WD, Wu F, Li JJ, You ZX (2017) Dispersion–precipitation synthesis of highly active nanosized Co$_3$O$_4$ for catalytic oxidation of carbon monoxide and propane. Appl Surf Sci 411:136–143
23. Marco P, Samir B, Debora F, Nunzio R (2016) Nanostructured ceria-zirconia catalysts for CO oxidation: study on surface properties and reactivity. Appl Catal.B 197:35–46
24. Zhang J, Peng WQ, Chen ZH, Chen H, Han LY (2013) Energy band tunable Ti$_x$Sn$_{1-x}$O$_2$ photoanode for efficient non-TiO$_2$ type dye sensitized solar cells. J Mater Chem A 1:8453–8463
25. Hirano M, Dozono H, Kono T (2011) Hydrothermal synthesis and properties of solid solutions and composite nanoparticles in the TiO$_2$-SnO$_2$ system. Mater Res Bull 46:1384–1390
26. Song MG, Wang YS, Guo Y, Wang L, Zhan WC, Guo YL, Lu GZ (2017) Catalytic wet oxidation of aniline over Ru catalysts supported on a modified TiO$_2$. Chin J Catal 38:1155–1165
27. Murayama T, Haruta M (2016) Preparation of gold nanoparticles supported on Nb$_2$O$_5$ by deposition precipitation and deposition reduction methods and their catalytic activity for CO oxidation. Chin J Catal 37:1694–1701
28. Chang LH, Chen YW, Sasirekha N (2008) Preferential oxidation of carbon monoxide in hydrogen stream over au/MgO$_x$-TiO$_2$ catalysts. Ind Eng Chem Res 47:4098–4105
29. Okal J, Zawadzki M (2013) Catalytic combustion of methane over ruthenium supported on zinc aluminate spinel. Appl Catal A 453:349–357
30. Wilburn MS, Epling WS (2017) Sulfur deactivation and regeneration of mono- and bimetallic Pd-Pt methane oxidation catalysts. Appl Catal B 206: 589–598
31. Lu M, Du H, Wei B, Zhou J, Li MS, Shan YH, Shen JY (2017) Hydrodeoxygenation of Guaiacol on Ru catalysts: influence of TiO$_2$-ZrO$_2$ composite oxides supports. Ind Eng Chem Res 56:12070–12079
32. Yao XJ, Yu Q, Ji ZY, Lv YY, Cao Y, Tang CJ, Gao F, Dong L, Chen Y (2013) A comparative study of different doped metal cations on the reduction, adsorption and activity of CuO/Ce$_{0.67}$M$_{0.33}$O$_2$ (M=Zr^{4+}, Sn^{4+}, Ti^{4+}) catalysts for NO+CO reaction. Appl Catal B 130-131:293–304
33. Yu ME, Li CT, Zeng GM, Zhou Y, Zhang XN, Xie YE (2015) The selective catalytic reduction of NO with NH$_3$ over a novel Ce-Sn-Ti mixed oxides catalyst: promotional effect of SnO$_2$. Appl Surf Sci 342:174–182
34. Wang YH, Wang F, Song Q, Xin Q, Xu ST, Yu J (2013) Heterogeneous ceria catalyst with water-tolerant Lewis acidic sites for one-pot synthesis of 1,3-diols via Prins condensation and hydrolysis reactions. J Am Chem Soc 135: 1506–1515
35. Takeguchi T, Kunifuji A, Narischat N, Ito M, Noguchi H, Uosaki K, Mukai SR (2016) Ligand effect of SnO$_2$ on a Pt-Ru catalyst and the relationship between bond strength and CO tolerance. Catal Sci Technol 6:3214–3219
36. Dong LH, Liu LJ, Lv YY, Zhu J, Wan HQ, Liu B, Gao F, Wang XS, Dong L, Chen Y (2012) Surface structure characteristics of CuO/Ti$_{0.5}$Sn$_{0.5}$O$_2$ and its activity for CO oxidation. J Mol Catal A-Chem 365:87–94
37. Sun CZ, Dong LH, Yu WJ, Liu LC, Li H, Gao F, Dong L, Chen Y (2011) Promotion effect of tungsten oxide on SCR of NO with NH$_3$ for the V$_2$O$_5$-WO$_3$/Ti$_{0.5}$Sn$_{0.5}$O$_2$ catalyst: experiments combined with DFT calculations. J Mol Catal A-Chem 346:29–38
38. Yao XJ, Tang CL, Ji ZY, Dai Y, Cao Y, Gao F, Dong L, Chen Y (2013) Investigation of the physicochemical properties and catalytic activities of Ce$_{0.67}$M$_{0.33}$O$_2$ (M = Zr^{4+}, Ti^{4+}, Sn^{4+}) solid solutions for NO removal by CO. Catal. Sci. Technol. 3:688–698
39. Dong LH, Sun CZ, Tang CJ, Zhang B, Zhu J, Liu B, Gao F, Hu YH, Dong L, Chen Y (2012) Investigation of surface VO$_x$ species and their contributions to activities of VO$_x$/Ti$_{0.5}$Ti$_{0.5}$O$_2$ catalysts toward selective catalytic reduction of NO by NH$_3$. Appl Catal A 431-432:126–136
40. An JH, Wang YH, Lu JM, Zhang J, Zhang ZX, Xu ST, Liu XY, Zhang T, Gocyla M, Heggen M, Dunin-Borkowski RE, Fornasiero P, Wang F (2018) Acid-promoter-free ethylene methoxycarbonylation over Ru-clusters/ceria: the catalysis of interfacial Lewis acid-base pair. J Am Chem Soc 140:4172–4181
41. Huang HF, Jiang B, Gu L, Qi ZH, Lu HF (2015) Promoting effect of vanadium on catalytic activity of Pt/Ce-Zr-O diesel oxidation catalysts. J Environ Sci 33: 135–142

42. Munoz-Batista MJ, Nasalevich MA, Savenije TJ, Kapteijn F, Gascon J, Kubacka A, Fernández-Garcia M (2015) Enhancing promoting effects in g-C_3N_4-Me^{n+}/CeO_2-TiO_2 ternary composites: photo-handling of charge carriers. Appl Catal B 176-177:687–698

43. Wang G, You R, Meng M (2013) An optimized highly active and thermo-stable oxidation catalyst Pd/Ce-Zr-Y/Al_2O_3 calcined at superhigh temperature and used for C_3H_8 total oxidation. Fuel 103:799–804

44. Xie SH, Liu YX, Deng JG, Zhao XT, Yang J, Zhang JF, Han Z, Arandiyan H, Dai HX (2017) Effect of transition metal doping on the catalytic performance of Au–Pd/3DOM Mn_2O_3 for the oxidation of methane and o–xylene. Appl Catal B 206:221–232

45. Basile F, Benito P, Fornasari G, Gazzoli D, Pettiti I, Rosetti V, Vaccari A (2009) Ni-catalysts obtained from silicate intercalated HTlcs active in the catalytic partial oxidation of methane: influence of the silicate content. Catal Today 142:78–84

46. Osman AI, Meudal J, Laffir F, Thompson J, Rooney D (2017) Enhanced catalytic activity of Ni on η-Al_2O_3 and ZSM-5 on addition of ceria zirconia for the partial oxidation of methane. Appl Catal B 212:68–79

47. Merino NA, Barbero BP, Grange P, Cadús LE (2005) $La_{1-x}Ca_xCoO_3$ perovskite-type oxides: preparation, characterisation, stability, and catalytic potentiality for the total oxidation of propane. J Catal 231:232–244

48. Elmasides C, Kondarides DI, Neophytides SG, Verykios XE (2001) Partial oxidation of methane to synthesis gas over Ru/TiO_2 catalysts: effects of modification of the support on oxidation state and catalytic performance. J Catal 198(2):195–207

49. Panagiotopoulou P, Kondarides DI, Verykios XE (2012) Mechanistic aspects of the selective methanation of CO over Ru/TiO_2 catalyst. Catal Today 181(1):138–147

50. Komanoya T, Kinemura T, Kita Y, Kamata K, Hara M (2017) Electronic effect of ruthenium nanoparticles on efficient reductive amination of carbonyl compounds. J Am Chem Soc 139(33):11493–11499

Publisher's Note

Springer Nature remains neutral with regard to jurisdictional claims in published maps and institutional affiliations.